Impact dynamics of the L chondrites' parent asteroid

Marine Ciocco, Mathieu Roskosz, Béatrice Doisneau, Olivier Beyssac, Smail Mostefaoui, Laurent Remusat, Hugues Leroux, Matthieu Gounelle

Impact dynamics of the L chondrites parent asteroid

Marine CIOCCO[1*], Mathieu ROSKOSZ[1], Béatrice DOISNEAU[1], Olivier BEYSSAC[1], Smail MOSTEFAOUI[1], Laurent REMUSAT[1], Hugues LEROUX[2] and Matthieu GOUNELLE[1]

[1]Institut de Minéralogie, de Physique des matériaux et de Cosmochimie (IMPMC), CNRS - UMR 7590, Sorbonne Université, MNHN, 75005 Paris, France.

[2] Univ. Lille, CNRS, INRAE, Centrale Lille, UMR 8207 - UMET - Unité Matériaux et Transformations, F-59000 Lille, France

*corresponding author. E-mail: marine.ciocco@mnhn.fr

Abstract – The dynamics of collisional events have been studied for three highly shocked L chondrites (Tenham, Sixiangkou and Acfer 040). Crystal growth rates of high-pressure polymorphs of olivines and pyroxenes and diffusion-driven redistribution of Mn, Ca, Fe and Na associated with these polymorphic transitions were studied independently. These two approaches were then applied on the same samples, and for meteorites that underwent different collisional histories. The relevance of the use of pyroxene polymorphs (*e.g.* akimotoite) is demonstrated. Combined analysis of the exact same ringwoodite and akimotoite crystals by Scanning Transmission Electron Microscopy (STEM) and NanoSIMS demonstrate that while STEM has a better lateral resolution, the 40nm maximum resolution of the NanoSIMS is sufficient to distinguish and analyze diffusion profiles. With STEM chemical and structural information concerning the nucleation mechanisms of ringwoodite and akimotoite, the concentration profiles derived from NanoSIMS images were used to derive the shock pulse duration and impactor size for these three meteorites. The two approaches (crystal growth kinetics and elemental diffusion) provide comparable durations assuming that diffusion coefficients are carefully selected. We obtain shock timescales of 1, 7 and 4 seconds for Tenham, Sixiangkou and Acfer 040, respectively. Corresponding impactor sizes are also calculated, and the results point towards either: (i) an early separation of the L chondrites from the parent body, and secondary impacts resulting in the observed meteorites or (ii) the meteorites all originate from different depths in the parent body.

1. INTRODUCTION:

High velocity collisions shaped the solar system all along its history and still trigger meteoritic ejection from their parent asteroid and fall on Earth. In this context, all asteroids and therefore all meteorites have gone through at least one impact. Meteorites can record these collisional events in their crystalline microstructure and mineralogy. Crystal defects, changes in mineral optical properties, shock veins and high-pressure (HP) polymorphs are typical indicators of such events (Stoëffler et al. 1991, 2018; Gillet et al., 2013)). High-pressure minerals are arguably the most iconic shock criterion as they unequivocally indicate extreme pressure conditions that cannot prevail in small planetary bodies. These mineralogical properties can also help to constrain the pressure, temperature, time (P, T, t) path during and in the aftermath of the collision.

Several estimates of the P, T conditions recorded by meteorites during impacts have been derived from shocked minerals in meteorites (e.g. Dodd and Jarosewich 1979; Chen et al. 1996; Sharp et al. 1997; Tomioka and Fujino 1997; Langenhorst and Poirier 2000; Chen et al. 2004). In the past decades, a few studies went a step forward and proposed estimates of shock pulses durations and impactor dimensions using various methods (e.g. Ohtani et al., 2004; Chen et al. 2004, 2006; Beck et al., 2005; Xie et al. 2006; Miyahara et al. 2010). Specifically, ringwoodite (the main HP polymorph of olivine) was used as a proxy for the determination of shock pulse durations. Othani et al., 2004 and Chen et al., 2004 studied its growth rates based on experimental data (Mosenfelder et al., 2001; Kerschoffer et al. 1998, 2000). Beck et al. (2005) expanded this method with the examination of elemental redistribution during olivine-ringwoodite solid-state transition, and focused on trace element diffusion between the ringwoodite lamellae and host olivines.

These approaches allowed them to estimate the lower limit of the shock pulse duration, ranging from 40ms (Xie et al. 2006) to several seconds (Chen et al. 2006). This discrepancy may be due to (i) a large variability in the asteroidal shock dynamics or to (ii) ambiguities in data processing and/or interpretations. For example, several aspects of data processing might have been overlooked. The spatial resolution of the analytical methods used to measure compositional gradients (NanoSIMS and Scanning Electron Microscope (SEM)) may induce large uncertainties on the inferred timescale. Furthermore, timescales derived from crystal growth and diffusion strongly depend on the actual mechanisms involved, and diffusion coefficients in literature which depend on thermodynamical parameters (*e.g.* oxygen fugacity, silica activity) and mineral compositions (Chakraborty, 2010). Finally, all data so far have been limited to ringwoodite. Therefore, the available literature data may not be totally appropriate to investigate high pressure polymorphs found in meteorites.

Here, we present evaluations of the shock duration as well as the impactor size for three different L chondrites: Tenham, Sixiangkou, and Acfer 040 which are known to contain a broad variety of high pressure polymorphs (*e.g.* Price et al. 1979; Sharp et al. 1997; Tomioka and Fujino 1997; Chen et al. 2004; Xie et al. 2006; Chen and Xie 2008). We focus on ringwoodite and, for the first time, on akimotoite (a common HP polymorph of pyroxene) present in these samples. The microstructure and phase relationships of the polymorphic assemblages were studied both by SEM and Scanning Transmission Electron Microscopy (STEM) in order to better understand growth mechanisms involved in these samples and to alleviate any methodological bias. Then chemical profiles measured by STEM-Energy Dispersive X-Ray Spectroscopy (EDX) and NanoSIMS on the same areas were compared in order to assess the spatial resolution of the NanoSIMS. A self-consistent array of timescales is

derived for each meteorite. We thus provide a '*toolbox*' to decipher the collisional history of the Solar System.

2. SAMPLES AND ANALYTICAL METHODS

2.1. Sample Choice

The L6 chondrites tend to statistically exhibit higher shock stages than other chondrite groups (Bischoff et al. 2018, Miyahara et al., 2021). Furthermore, although several studies seem to indicate a catastrophic breakup event of the L chondrites parent body occurred about 470 Ma ago (Korochantseva et al. 2007, Swindle et al. 2014, Schmitz et al. 2001), the dynamics of this impact are still not constrained. In addition, recent studies suggest that there were at least two L-parent bodies at the time of the collision (Jenniskens et al., 2019). More insights on the dynamics of the collisions could allow us to draw some clues about the number or stratification of L chondrites parent body(ies) and their history.

Thin sections of Sixiangkou, Acfer 040 and Tenham were investigated. These meteorites are well characterized and contain abundant shock veins and high-pressure minerals. Tenham fell in Australia in 1879 and has been classified as L6. A variety of high pressure minerals were discovered inside its shock veins, including ringwoodite (Binns et al. 1969), akimotoite (Tomioka and Fujino 1997) and bridgmanite (Tomioka and Fujino (1997) ; Tschauner et al. 2014). As far as shock timescales are concerned, Tenham has been previously studied by Beck et al. (2005) and Xie et al. (2006). Two thin sections were studied here. One (MNHN 3381lm1) was prepared from a 150 g stone at the Muséum National d'Histoire Naturelle de Paris (MNHN). Another one (PL94197) was borrowed from the Münster Institut für Planetologie (IFP). Sixiangkou fell in 1989 in Jiangsu (China) and has been classified as L5 or L6 (e.g. Wang et al., 1995; Wlotzka, 1990; Chen et al., 2006). One thin section was borrowed from the University of California, Los Angeles (UCLA). Finally, Acfer 040 was found in Tamanghasset (Algeria) in 1989 and has been classified as L5-6 (Bischoff and Geiger, 1995). It is one of the first meteorites were akimotoite was found (Sharp et al., 1997; Tomioka and Fujino (1999)). The studied section (PL19012) was borrowed from the IFP.

2.2 Sample preparation

All the sections were carbon coated before chemical analyses. 25 nm of carbon was deposited onto their surfaces. In order to perform STEM analyses, focus ion beam FIB sections were prepared from these thin sections. The firsts two were collected from Tenham and Acfer 040 and prepared at IMPMC (Institut de Minéralogie, de Physique des Matériaux et de Cosmochimie), on a Zeiss Neon40EsB equipment. Before milling, a platinum strap was deposited onto the region of interest. Then, the initial milling steps, consisting of a rough excavation from both sides of the thin foil were operated with a Ga+ beam at 30kV and 2nA, decreasing the current when the milling is getting close to the foil. Then, a micromanipulator was used to weld the foil onto a M-shaped copper grid. The remaining section was then thinned down by decreasing the current till the end with a 100pA ion current on both sides of the foil in order to reach a thickness of about 100nm. These sections were strictly used for STEM analyses. Two other sections were engineered at IEMN, Lille, France, using the FEI strata DB 235 FIB-SEM. Great care was taken to avoid structural modification of these sections, as they were chosen for the STEM-NanoSIMS comparison. Upon completion of the STEM measurements, the FIB sections were then recovered from the copper grids and deposited to an aluminum holder. They were then carbon coated to perform NanoSIMS analyses.

2.3 Analytical Methods

2.3.1. Optical Microscopy

The initial examination of the samples was conducted through a Leica optical microscope, in transmitted and reflected light. This first survey of the shock veins allowed to locate the biggest, most distinguishable (*i.e*. colored in natural light) high pressure polymorphs and the areas where the shock effects were the most prevalent.

2.3.2. Raman Spectroscopy

Raman spectroscopic analyses were carried out using a continuous-wave (CW) Raman microspectrometer Renishaw InVia Reflex (IMPMC). Measurements were performed using a green 532 nm solid-state laser focused on the sample through a Leica DM2500 microscope with a long-working distance 50X objective (NA = 0.55). This configuration yields a planar resolution of ≈1-2 µm for a laser power delivered at the sample surface set at less than 9 mW using neutral density filters to prevent irreversible thermal damages. This corresponds to a laser irradiance in the range of 0.3-1.3 10^9 $W.m^{-2}$. All measurements were performed with a circularly polarized laser using a ¼-wave plate placed before the microscope in order to minimize polarization effects. The Raman signal was dispersed by a grating with 2400 lines/mm and the signal was analyzed with a RENCAM CCD detector. The spectral resolution for visible light was 1–1.9 cm^{-1} and the wavenumber accuracy was better than 0.5 cm^{-1}. The acquisition times ranged between 60 seconds and 5 minutes.

2.3.3. Scanning Electron Microscopy

Detailed textural analyses were performed at the IMPMC. These measurements were performed on a Zeiss Gemini SEM. The images were taken with the Angle Selective Backscattered detector in the following conditions: 15kV accelerating voltage, 7.5mm working distance with the Angle Selective Backscattered detector, aperture of 60 µm and High Current. Energy Dispersive Spectroscopy analyses and chemical maps were also acquired in those conditions. SEM was mainly used for a first-order characterization of mineral assemblages, as well as the dimensions of the microstructures. Indeed, SEM pictures were used to measure the width of the high-pressure polymorphs and to select the most adapted crystals for detailed studies by NanoSIMS and (S)TEM, this was done using reference pictures and the software The Gimp. We estimate the error to be around 0.3 µm, which is the size of the pixel on most of our images.

2.3.4. Electron Microprobe Analysis

Chemical maps of most thin sections were collected on a CAMECA SX 100 EPMA (École Nationale Supérieure de Chimie, Lille, France). The TaP, LLIF and LPET crystals were used for measurements. Typically, SiO_2, FeO, Na_2O, TiO_2, Al_2O_3, MnO, CaO, MgO and Cr_2O_3 concentration maps were collected on different regions for each meteorite. Measurements were performed at a 15 keV voltage, with a dwell time of 2 seconds per pixel. In addition, several concentrations profiles and point analysis were performed in multiple regions of interest.

2.3.5. NanoSIMS

High-resolution compositional maps were also collected on the NanoSIMS 50 installed at MNHN (Paris, France), equipped with a Radio Frequency (RF) Plasma O source. The RF Hyperion-II Plasma ion source is an upgrade from the duoplasmatron. Its particularity is the beam density, 6 to 10 times higher than the duo, resulting in a better spatial resolution (comparable to the Cs source) while still using O^- ions (Malherbe et al., 2016; Liu et al., 2018).

Each map was collected after a pre-sputtering of 15 to 25 minutes with a primary current of about 120 pA on a 20x20 to 50x50 squared microns area. A current of about 10 pA on areas varying from 40x40 to 15x15 µm was applied for the actual measurements. The $^{24}Mg+$, $^{44}Ca+$, $^{27}Al+$, $^{27}Si+$, $^{23}Na+$, $^{39}K+$, $^{55}Mn+$ and $^{56}Fe+$ secondary ions were collected simultaneously using the combined analysis mode. The main standards used for calibration of the maps were the San Carlos olivine and a San Carlos orthopyroxene. Mass table was set up using relevant samples: San Carlos Olivine for Fe, Mg, and Si; Apatite for Ca, Rhodonite for Mn, Orthose for K, Corundum for Al and Aegyrine for Na. Data processing, extraction of concentration profiles, standard error and evaluation of the spatial resolution were performed using the software LIMAGE. The profiles are integrated over 10 pixels wide. For each area of interest, multiple profiles were taken along the length of the structures. The profile lengths were then averaged to calculate the corresponding shock pulse for the diffusion considered. As for the TEM-NanoSIMS comparison, the NanoSIMS analyses focused on zones ranging from 8 to 5 square microns. Care was taken to have a current as low as possible and a beam size as small as possible. The current was kept under 1 pA for analysis and under 100 pA for pre-sputtering. Between 50 to 100 planes were acquired on each area, depending on the section thickness.

2.3.6. Transmission Electron Microscopy (TEM)

Tenham and Acfer 040 were also observed by transmission electron microscopy. The thin sections prepared at the IMPMC were studied on a Jeol 2100F TEM. Chemical maps and profiles were acquired for up to 1 hour, and images were taken in scanning TEM (STEM) mode with a tension operating at 200 kV, with a dwell time of 0.1 ms. The thin sections fabricated in Lille were investigated on a Titan Themis 300 TEM equipped with a four-quadrant, windowless, super-X SDD EDX detector. Chemical maps were acquired at 300 keV with a beam current of 0.2 nA and a convergence angle of 20 mrad. The duration of acquisitions extends for up to 5 hours (for Acfer 040) and up to 3 hours (Tenham). Quantified chemical profiles were extracted from the chemical maps and were computed by the quantification tool of the Bruker Esprit® software. The sections meant to be compared with NanoSIMS were first analyzed in TEM to minimize ablation of the surface material and inaccurate superposition of the profiles.

2.4 Shock Pulse Calculations

Once the measurements were performed, the multiple diffusion profiles were taken into account for each considered assemblage. A mean value was used for the calculations in the models. The method of shock pulse calculation used here is similar to the one detailed in Beck et al. (2005). It consists in tracing concentration profiles for several minor elements on interfaces between a high and a low-pressure polymorph. As the structure of the two minerals slightly differs, some elements might be incompatible within the crystalline lattice of one or the other polymorph. Thus, the concentrations of these elements will be slightly different between the two minerals: a concentration gradient of certain elements is visible near the interface between the two polymorphs. The use of this method is based on the assumption that the element partitioning only occurred during the shock pulse, hence the value of the shock pulse is naturally superior to the time required for the diffusion to happen.

3. RESULTS

3.1 Shock veins mineralogy

The three meteorites exhibit fairly similar mineralogies and have the typical compositions and modal abundances of L chondrites (Kallemeyn et al., 1989). They are all dominated by olivine ($Fo_{\sim 70}$) and also present abundant pyroxene (Table 1). Other secondary components are iron-nickel alloys, troilite, chromite, apatite and whitlockite.

In the shock veins of the three meteorites, ringwoodite is by far the most common high pressure mineral. Its composition is generally similar to that of host olivines (Fo_{65-70}). Other common minerals in veins and their vicinities include akimotoite, orthopyroxene and glass with plagioclase compositions, droplets of iron-nickel alloys, sulfides, magnetite, as well as garnet with composition lying along the majorite-pyrope solid solution and including some pure majorite. Accessory minerals include chromite, apatite and whitlockite. Wadsleyite, the intermediate pressure polymorph of olivine, is only found as remnants on ringwoodites raman spectra. Untransformed olivine is sometimes present as an accessory mineral in the melt veins in Tenham and Acfer 040. Hollandite-type plagioclase (the composition of which is close to lingunite) is found in Tenham and Sixiangkou. No crystalline plagioclase was found in any of the veins. Moreover, no bridgmanite could be unambiguously identified in our sections. In order to identify a potential composition for the impactors, xenoliths were searched in the chondritic part of the samples. The samples were entirely mapped via EDX but no particular areas presenting drastic chemical differences were detected. This is consistent with the observation that L ordinary chondrites contain very few xenoliths (Briani et al., 2012; Marrocchi et al., 2021).

3.2 Microstructures and phase relationships

3.2.1. Ringwoodite-Olivine assemblages

The prevalent microstructure of ringwoodite consists of polycrystalline aggregates, up to several hundred microns large (Fig. 1.A). Under the optical microscope, its color varies from brown, blue, to colorless (the most common). These crystals are also found in the melt vein matrix. In addition to this dominant microstructure observed in all studied meteorites, Tenham and Sixiangkou present lamellar ringwoodite whereas Acfer presents a more uncommon ringwoodite-olivine assemblage.

Ringwoodite lamellae found in Tenham and Sixiangkou are associated to large olivine crystals. Based on BSE images, these lamellae appear brighter compared to the surrounding olivine crystals (Fig. 1.B). In Tenham, the largest lamellae exhibit a complex microstructure: a fine-grained center surrounded by coarser non-oriented crystals (Fig 2.A). Thinner lamellae, do not show this association with coarse grains. Moreover, for these lamellae, dark-field TEM observations coupled to conventional electron diffraction reveal a preferred orientation relative to the host olivine grains. This suggests a coherent growth mechanism. Coarser grains did not show any preferential orientation, pointing to an incoherent growth mechanism.

A similar microstructure was found in Sixiangkou with discontinuous, polycrystalline and wavy lamellae, reminiscent of the coarser grains observed in Tenham (Fig. 1.B). The exact structural relationship between olivine and ringwoodite is still unclear suggesting that crystal growth in Sixiangkou is incoherent (see also Chen et al 2006).

The sizes of lamellae were measured in order to derive shock pulses. In Tenham, the lamellae are usually between 1 and 3 µm wide with an average value of 2.2 µm (±0.4, n=26, see Table 2), whereas in Sixiangkou, they tend to be thinner with an average value of 1.4 µm (±0.1, n=5) (Fig. 1.B.).

Ringwoodite-olivine assemblages are very different in Acfer 040. In addition to polycrystalline aggregates, ringwoodite is also found as iron-rich rims around pre-existing olivines (Fig 1.A.). They may in some cases correspond to the iron endmember of the ringwoodite solid solution (namely ahrensite). Furthermore, olivines can also present a fibrous texture (Fig. 1.A.). The TEM observations of Acfer 040 only focused on akimotoite (see below), due to the lack of ringwoodite lamellae.

3.2.2. Akimotoite-pyroxene-glass assemblages

Akimotoite occurs mainly as small aggregates, generally below 10 µm wide. However, akimotoite presents other microstructures. Hints of akimotoite were detected in the melted matrix by Raman spectroscopy but most of the time, it is found associated with its low-pressure pyroxene polymorph (Fig 1.C.; 3). In very rare cases (only one occurrence identified in Tenham), akimotoite was also encountered as lamellae akin to those described for ringwoodites (Fig. 1.D.). These lamellae appear more regular in size distribution than those reported in Ferroir et al. (2008). We found a maximum width of 0.9 µm, with an average value of 0.8 µm for 5 different lamellae. Finally, a third microstructure is common in Acfer 040 (Fig. 1.E), and was previously described in Sharp et al., 1997 and Feng et al., (2017). This texture is composed of patches of akimotoite crystallites embedded in a $MgSiO_3$ composition glass (Fig 2.B). The width of these patches can reach almost 7 µm wide.

3.3 Chemical redistribution during shock-induced phase transitions

Both major and minor elements are redistributed during olivine-ringwoodite and pyroxene-akimotoite phase transitions. Such redistribution (or partitioning) is controlled by the rapid change in the crystal structure. In this context, the transient nature of the shock prohibits thermodynamical and compositional equilibrium to be reached. As a consequence, the gradients observed in minerals are essentially diffusion profiles. They can even be observed on BSE images for some major elements. However, in the case of minor elements, STEM-EDX and NanoSIMS resolution were required. NanoSIMS potentially offers a higher sensitivity for trace and light (or volatile) elements, an easier sample preparation, and larger sample sizes and survey coverages than STEM. However, its spatial resolution is expected to be lower than TEM and notoriously difficult to evaluate in practice. For this reason, we first compare the resolution of these two instruments on exactly the same samples.

3.3.1. Evaluation of the NanoSIMS spatial resolution

The NanoSIMS and TEM chemical profiles were collected for both ringwoodite-olivine and akimotoite-glass assemblages in Tenham and Acfer 040 (Fig. 4). Profiles were collected on the same locations and the same FIB sections. We note however that some degree of sputtering and amorphization was inescapable during a prolonged STEM-EDX analysis. Overall, the shapes of the profiles are remarkably similar. As far as the glass-akimotoite assemblages are concerned, the NanoSIMS captures actual chemical fluctuations with the same level of detail as STEM-EDX. This is especially true for Mn, Mg, and Na in akimotoite. Some slight differences may be found in the Ca and Fe profiles (Fig. 4). The agreement is slightly lower in the case of the ringwoodite-olivine. The widths of NanoSIMS profiles are either comparable or slightly larger than those measured by STEM (Fig. 4). As an example, the width of the Mn NanoSIMS profile is larger than the STEM-EDX profile by about 13%. This misfit is however lower than the typical error associated with the second approach followed in literature to determine shock pulses (i.e. the crystal width measured by SEM, with a typical uncertainty of

20%). In conclusion, NanoSIMS spatial resolution is suitable to derive accurate shock timescales.

3.3.2. Chemical redistributions

Most ringwoodites display enrichments in Fe and correlated depletions in Mg as compared to the parent olivine. At a finer scale, lamellae can also present these zonations in Fe and Mg (Fig. 5). However, the most striking and consistent chemical feature is the depletion of Mn observed in all ringwoodites by EPMA, TEM-EDX and NanoSIMS (Fig. 6). Between host olivine and ringwoodite, the decrease is typically of the order of 10% (from 0.45 wt% MnO in olivine to 0.40 wt% in ringwoodite). Such depletion was previously reported in Beck et al. (2005). Distribution of Ca, Al, Na, K, Ti and Cr did not show measurable variations in ringwoodite. The diffusion length observed for these assemblages is generally proportional or equal to the width of lamellae, the largest Mn diffusion distance being over 3 µm and the smallest measurement being 0.76 µm. In Tenham, in average, the length is 2.4 µm, whereas in Sixiangkou, we report an average of 1.4 µm, matching the lamellae width.

In akimotoite lamellae, both TEM and NanoSIMS measurements show that Fe tends to be enriched (relative to the glass) so are minor elements such as calcium and sodium. This seems in good agreement with the observations of Ferroir et al. (2008), although in the present study, no increase in aluminum concentration is noted. The diffusion features in the lamellar texture of Tenham were less extended than in ringwoodite lamellae, with a maximum of 1.5 µm and a minimum of 0.6 µm for sodium. Over the 5 studied lamellae, the average diffusion length was 1.1 µm. Akimotoite crystals in Acfer 040 appear depleted in iron, manganese, calcium and sodium compared to the surrounding glass. On the other hand, they are enriched in magnesium and silicon. The concentration of the melt in elements such as manganese, sodium and iron is similar to that of the nearby vein matrix (Fig. 6.C). From these data and despite the obvious lack of bulk thermodynamical equilibrium of the system, it may be interesting to derive apparent partition coefficients between akimotoite and melts. These values should not be taken as face values but still may represent reasonable first order approximations of true partition coefficients. We calculate glass-akimotoite coefficients in Acfer 040 following the equation $K_{app}=C_{aki}/C_{melt}$ (Table 3).

4. DISCUSSION

4.1 Transformation mechanisms

Given the substantial dimensions of most of the aggregates in our samples, the chemical similarities with the host olivines, and the abundance of the lamellar texture, where olivine and ringwoodite are both present with no trace of melting, the majority of ringwoodites must have transformed through a solid-state mechanism. Previous experimental works (e.g. Kerschoffer et al. 1998, 2000) describe the formation of the lamellae as a combination of a shear process and a short phase of coherent nucleation and growth, followed by a dominant phase of incoherent growth. The lamellae in Tenham and Sixiangkou are larger than those produced experimentally, and present compositional changes. Our observed structures are nonetheless consistent with a two-phased process (Fig 2.A), despite the fact that there is no evidence that the inner part of the lamellae are coherent with the olivine matrix. The coarser crown is, however, clearly incoherent. It is likely that the inner, finely grained lamellae crystallized on fractures within olivine crystal, and that a slightly different process led to the incoherent nucleation of the coarse outer polycrystals. This mechanism could be similar to what is observed in Chen et al. (2006).

The mechanisms might be different for akimotoite. In Tenham, the lamellar texture most likely corresponds to a solid-state transformation, possibly a shear mechanism as detailed by Tomioka (2007). The smallest aggregates of Tenham and Sixiangkou might have crystallized from a melt, because some minerals include higher concentrations of alkali elements (Table 1). These enrichments may derive from mixing of the molten pyroxene with the surrounding shock melt vein liquid and subsequent crystallization.

As for the $MgSiO_3$ glass-crystallite akimotoite assemblage in Acfer 040, this formation is more ambiguous. The textures observed are not compatible with the traditional hypothesis that the $MgSiO_3$ glass originates from bridgmanite amorphization (Tomioka and Fujino, 1997; Sharp et al., 1997) because there are no back transformation features nor cracks around the glass precursor. The glass is extremely homogeneous in composition, making it unlikely to form by the backtransformation of a former aggregate. Feng et al. (2017) provided another scenario for the GRV 052082 L6 chondrite that could explain both the depletion of many elements in akimotoite as well as the textures observed here. The melting of a pyroxene, and subsequent fractional crystallization of the akimotoite from this melt would reproduce the observed chemical properties of akimotoite. Nonetheless, the assemblage in Acfer 040 presents more pronounced and diverse elemental fractionation than GRV 052082. Likewise, the olivine with intergrown ringwoodite textures observed in Acfer 040 in the present study are very similar to those attributed to fractional crystallization in the Peace River meteorite by Miyahara et al. (2009), although their team report wadsleyite along with the two other polymorphs of olivine.

4.2 Recorded P-T-t path of the shock

All the investigated meteorites have been studied previously. Here, we attempt to refine the interpretations made in the early 2000s in light of our additional measurements. First, pressure peak in Tenham was estimated to have reached 45 GPa by early studies (Price et al. 1979), and was refined in the 2000s by Beck et al. (2005) and Xie et al. (2006) to be between 21 and 25 GPa. Since crystalline bridgmanite was discovered in the melt vein by Tschauner et al. (2014), it is assumed that the pressure must have reached at least 24 GPa, according to the pressure temperature diagram available in Tomioka and Miyahara (2017).

The ubiquitous akimotoite lamellae in Tenham imply that the P-T-t path followed by this meteorite was unique: either the time scale was long enough to allow local transformation of the pyroxene into akimotoite lamellae which is more sluggish than the olivine-ringwoodite transition (Zhang et al., 2006, Hogrefe et al., 1994), or that the pressure and temperature were particularly high to speed up this uncommon transformation. Shearing could also play a significant role (Tomioka et al 2007), but cannot explain entirely the observed chemical partitions.

As for Acfer 040, it was inferred that some nanocrystals in the matrix matched the crystallographic patterns of synthetic $MgSiO_3$ perovskite suggesting a peak pressure larger than 24 GPa (Sharp et al. 1997). The main characteristic feature of Acfer 040 is its abundant localized fractional crystallization assemblages, that points towards a slightly different P-T-t path. The initial temperature might have been as high as 2700 K, causing pyroxene melting (Feng et al., 2017). Then, the pressure and temperature conditions lasted longer, allowing for local crystallization of akimotoite in the confined melt.

Finally, in the Sixiangkou meteorite, no bridgmanite has been found in this study nor reported in the literature. This implies that the pressure was not higher than 24 GPa, as bridgmanite dominates the $MgSiO_3$ stability diagram above this pressure (Tomioka and Miyahara 2017). There was no molten pyroxene apparent, nor signs pointing towards volume changes. Nonetheless, in this meteorite, no trace of olivine, olivine/ringwoodite assemblage, nor wadsleyite was found directly inside the shock veins (contrary to Acfer 040 and Tenham). Therefore, we assume that the pressure distribution was more homogeneous in the veins of Sixiangkou. Furthermore, given the abundance of polymorphs and complete lack of olivine in the melt vein, the pressure was likely right below the bridgmanite stability domain.

The samples contained akimotoite, often accompanied by majorite, which according to the phase diagram of $MgSiO_3$, implies a temperature at least locally superior to 2000 K (Sawamoto 1987). Furthermore, melting experiments on the KLB-1 peridotite and Allende (Agee et al. 1995) indicate that these two samples respectively melted at 2573 and 2373 K at a pressure of above 24GPa. Given the composition (especially the forsterite percentage) of olivine, we infer that the liquidus temperature is closer to the Allende meteorite, hence about 2400 K. The presence of lingunite in Sixiangkou and Tenham suggests a temperature around 2250 to 2450 K (Wang and Takahashi 1999). Finally, according to Litasov et al. (2019), the triple point majorite-akimoite-bridgmanite is around 2400 K as well. Therefore, we choose a temperature of 2400 K for our calculations, for all meteorites. However, given the wide range of polymorphs observable in all of the veins, it is clear that the temperature was quite heterogeneous. Thus, we present results as a function of the temperature.

4.3 Shock Pulse Algebra and choice of Diffusion and growth constants

With the newly obtained data, and knowing the diffusivities for different elements, time needed to form the observed diffusion profiles can be estimated from simple diffusion equations:

$$x(t) = \sqrt{t \cdot D_0 \cdot e^{\frac{-Ea}{TR}}} \quad , \tag{1}$$

which gives us:

$$t = \frac{x^2}{D_0 e^{-\frac{Ea}{RT}}} \quad , \tag{2}$$

where *x* is the distance over which a given element diffused, *t* is the shock pulse duration, D_0 is the pre-exponential factor of the diffusion coefficient, E_a is the activation energy of the

diffusion, *T* is temperature and R is the gas constant. Similarly, the time needed for the ringwoodite lamellae to form can be estimated, using the growth rate equation as defined in Christian (1975):

$$\gamma = \frac{\Delta x}{\Delta t} = k_0 T \cdot e^{\frac{-\Delta Ga}{RT}} \cdot \left(1 - e^{\frac{\Delta Gr}{RT}}\right), \quad (3)$$

where γ is the growth rate, x is the lamellae width, k_0 is a constant, ΔGa is the activation energy of the considered transformation and ΔGr is the Gibbs free energy of the transformation. With these informations, the time required to form the lamellae can be determined as a function of T and would represent a lower limit to the shock pulse duration.

The diffusion and kinetic data used in this study are summarized in Table 4. As discussed in 4.1, the mechanism discussed in Kerschoffer et al. (2000) is assumed to be relevant for the ringwoodite formation. Therefore, the corresponding growth rate constants are used. Thermodynamic values of the olivine to ringwoodite transition were calculated in Akaogi et al. (1989). As for the diffusion coefficients, the Mn and Ca pre-exponential coefficient and activation energy are taken from Jurewicz et al. (1988). The diffusion coefficient of Ca has been extensively discussed in previous studies. Only Spandler and O'Neill (2010) find similar values. Cherniak and Dimanov (2010) or Coogan et al. (2005) did not confirm values from Jurewicz et al. (1988). Dohmen et al. (2017) attribute these discrepancies to experimental artifacts. We chose to use the values of Jurewicz et al. (1988) as they present estimations of both Mn and Ca, whereas other studies tend to assimilate Mn diffusion to Fe-Mg interdiffusion. Furthermore, proposed to interpret the differences in diffusion coefficient between Jurewicz et al. (1988) and others is the presence of melt surrounding the crystals speeding up diffusion (Bloch et al., 2019). If true then this configuration is closer to what is found in shock melt vein. The diffusion coefficients of Fe in pyroxenes are from Dimanov and Wiedenbeck (2006) because they were validated for higher temperatures than other studies. Finally, concerning Ca diffusion in pyroxene, we used the values of Brady and McCallister (1983) because the iron content of their starting samples matched the composition of our samples.

The strongest hypothesis in our model comes from these various diffusion and kinetic coefficients used in our calculations. They were indeed determined for the low-pressure polymorphs and thus might not capture completely the kinetics of processes recorded over 2000 K and 23 GPa. Furthermore, the values available for minor and trace element diffusion are determined for pyroxenes of diopside composition, whereas most of the pyroxenes in our meteorites are enstatite. Moreover, the shearing during the shock may facilitate the diffusion by creating local discontinuities in the host crystals (Greshake et al., 2013) but its effect has not been quantified. As for the growth rate considerations, the largest uncertainties lay on the application of coefficients determined for a transformation mechanism that might be different during impacts and in static experimental conditions. As an example, static experiments need several hours to form comparatively small (500 nm wide) polymorphs lamellae (Kerschoffer et al. 1998, 2000). Finally, while some values are available for the growth of ringwoodite, there are to our knowledge virtually no data on the kinetics of the enstatite-akimotoite transformation. Finally, one limitation of our model is the constant temperature assumption. The decrease in temperature during the adiabatic pressure drop is difficult to quantify. But clearly, this decrease would lead to underestimate the shock timescale. With these limitations in mind, we now derive main properties of the impactor and impacted bolides. For a temperature of 2400 K, we derive shock pulse durations of 1, 7 and 4 seconds respectively for Tenham, Sixiangkou and Acfer 040 (Figure 7). For Tenham and Sixiangkou, our values are close to that previously estimated (Beck et al. 2005; Chen et al. 2004).

4.4 Asteroids' sizes

With the determined shock pulse timescales, impactor diameters can be estimated using an empirical relation given based on the assumption that the shock wave propagates over a distance comparable to that the impactors' diameter (Melosh 1989). Therefore the impactor diameter (D_i) reads:

$$D_i = t \,.\, v \,, \tag{4}$$

where *t* is the shock pulse duration and *v* the relative velocity. Assuming a collisional speed of 5km/s (Bottke et al. 1994), the impactors that extracted the meteorites had diameters of 5, 30 and 22km, respectively.

Following the same first order simplification, a minimal size of the impacted asteroid can be inferred. In fact the very existence of shocked meteorites which have subsequently been produced demonstrate that the shocked asteroid survived the collision. Therefore, the kinetic energy of the impactor ($E = \frac{1}{2}mv^2$) cannot be larger than the gravitational binding energy of the impacted asteroid ($U = \frac{3GM^2}{5R}$) where *v* and m are the velocity and the mass of the impactor and *R* and M are the radius and the velocity of the impacted asteroid. Therefore,

$$\frac{3G{\rho_{pb}}^2 \cdot (\frac{4\pi}{3}{R_{pb}}^3)^2}{5R_{pb}} > \frac{1}{2} \cdot \rho_i \cdot (\frac{4\pi}{3}{R_i}^3) \cdot v^2, \tag{5}$$

where ρ denotes asteroidal density, *Pb* stands for the parent body properties and *i* the impactor properties. Because no xenoliths have been found in the meteorites, we can assume that both the impactor and the impactee have the same density yielding to:

$$R_{pb} > \sqrt[5]{\frac{\frac{5}{2}(t)^3 \cdot v^5}{3 \cdot (\frac{4\pi}{3}) \cdot G\rho_{pb}}}. \tag{6}$$

Using the impactors' diameters calculated above and a density of 3.5g/cm^3 implies that the parent bodies of Tenham, Sixiangkou and Acfer 040 must have been larger than 100, 300 and 240 km to avoid complete destruction. Although these simple empirical laws do not capture all the details of the collisions, the order of magnitude of the minimal radius scaling with v and the $\sqrt[5]{t^3}$ is probably correct. Impactor diameters have also been derived from shock pulses by Bowling et al. (2020) using a numerical modeling of impact shock physics. Authors also discussed the validity of Melosh' equation (1989). They compared their results to those obtained by Beck et al. (2005), who used Melosh's equation and concluded that this formula underestimates the impactor size by a factor of 8. It is however of note that their work is relevant to the Martian surface. This implies that the involved geometries is more complicated, because the ejected material would need to be at the impact point to see ejection speeds superior to Mars' escape velocity. On the contrary, material ejection from asteroids occurs under very different conditions since there is no significant gravity on these bodies. Given the uncertainties on the diffusion constants, the lamellae width, and the profile length, one can however consider that the size estimates for the three meteorites are, within error, identical and in the order of a few 100 km. This asteroidal size is in line with the idea that asteroids were born big (Morbidelli et al. 2009) and suggest that the collision endured by the L6 parent-asteroid and recorded by the three meteorites under study occurred in the early Solar System history. These values are also consistent with the determination of the radius of the L chondrite parent body made by Gail and Trieloff (2019) on the basis of a thermal model. Furthermore, our derived diameters are consistent with the recent theoretical study by Meier et al. (2017), suggesting that the Ino family might be the source of the L chondrites, (especially

the highly shocked ones). Alternatively, the reasonable mass of the Massalia family also proposed as the L chondrite parent body recently (Gaffey and Fieber-Beyer 2019; Strom et al. 2021), could be a possible candidate with its diameter of 150 km. Conversely, the Gefion family, initially proposed by Nesvorný et al. (2009), seems to be too small even if ~800% of the mass was lost during a catastrophic impact scenario.

5. CONCLUSION

The mineralogy of 3 highly shocked L chondrites (Acfer 040, Tenham, Sixiangkou) was investigated. Acfer 040, which was scarcely described in previous studies, displays a shock vein with different textures compared to Tenham and Sixiangkou. In the center of the vein, low pressure olivine still remains, amongst aggregates of ringwoodite and glassy assemblages of $MgSiO_3$ and high-pressure polymorphs. A first attempt to use these formations as a way to derive shock timescales was undertaken. For all meteorites, most transformations mechanisms involved are solid-state, either resulting in completely transformed aggregates of polymorphs, or formation of lamellae, but Acfer 040 presents notable amounts of fractional crystallization. NanoSIMS profiles used to characterize these transformations are close to the ones obtained by STEM-EDX. We determined shock timescales of 1, 7 and 4.5 seconds for Tenham, Sixiangkou and Acfer 040, respectively. In turn, this suggests that the impactor sizes were of the order of 5, 30 and 22 km and the size of the parent body of 100, 300 and 240 km to avoid *complete* destruction. Finally, the results obtained via the analysis of akimotoite lamellae match those obtained via ringwoodite lamellae in Tenham. Akimotoite is therefore promising to better constrain shock timescales, and to offer an alternative when ringwoodite is not available in a given sample. To consolidate this method, more experimental determinations of diffusion coefficients in high pressure silicate polymorphs are however mandatory.

6. Acknowledgements

We thank the two anonymous reviewers for their comments which improved this manuscript. We would like to thank Sylvain Pont as well as Imène Estève and Stéphanie Delbrel (IMPMC) for their assistance with the scanning electron microscopy. Séverine Bellayer (École Nationale Supérieure de Chimie de Lille) and her experience with the electron microprobe analysis highly contributed to this study. The expertise of David Troadec (IEMN, Université de Lille) was pivotal to the TEM measurements as he produced and manipulated the FIB sections. We also thank Maximilien Verdier-Paoletti (IMPMC) for his assistance with NanoSIMS treatment. We are grateful to François Guyot for his help with the transformation mechanisms. Finally, we deeply thank Addi Bischoff (Münster IFP) and Alan Rubin (UCLA) for the meteorite loans as well as Lionel Marié (CEREGE) for preparing some of the Tenham thin sections. HL thank I-SITE ULNE and the MEL for funding. The electron microscopy works at the University of Lille were done with the support of the Chevreul Institute, the European FEDER and Région Hauts-de-France.

7. References

Agee C.B., Li J., Shannon M.C. and Circone S. 1995. Pressure-temperature phase diagram for the Allende meteorite. *Journal of Geophysical Research: Solid Earth*, *100*(B9), pp.17725-17740.

Ashida T., Kume S., Ito E. and Navrotsky A. 1988. MgSiO 3 ilmenite: Heat capacity, thermal expansivity, and enthalpy of transformation. *Physics and Chemistry of Minerals*, *16*(3), pp.239-245.

Beck P., Gillet P., El Goresy A. and Mostefaoui S. 2005. Timescales of shock processes in chondritic and martian meteorites. *Nature*, *435*(7045), pp.1071-1074.

Binns R. A., Davis R. J., and Reed S. J. B. 1969. "Ringwoodite, natural (Mg, Fe) 2 SiO 4 spinel in the Tenham meteorite." *Nature* 221, no. 5184 : 943-944.

Bischoff A. and Geiger T. 1995. Meteorites from the Sahara: Find locations, shock classification, degree of weathering and pairing. *Meteoritics*, *30*(1), pp.113-122.

Bischoff A., Schleiting M. and Patzek M. 2019. Shock stage distribution of 2280 ordinary chondrites—Can bulk chondrites with a shock stage of S6 exist as individual rocks?. *Meteoritics & Planetary Science*, *54*(10), pp.2189-2202.

Bloch E.M., Jollands M.C., Gerstl S.S., Bouvier A.S., Plane F. and Baumgartner L.P. 2019. Diffusion of calcium in forsterite and ultra-high resolution of experimental diffusion profiles in minerals using local electrode atom probe tomography. *Geochimica et Cosmochimica Acta*, *265*, pp.85-95.

Bottke Jr W.F., Nolan M.C., Greenberg R. and Kolvoord R.A. 1994. Velocity distributions among colliding asteroids. *Icarus*, *107*(2), pp.255-268.

Bowling, T.J., Johnson, B.C., Wiggins, S.E., Walton, E.L., Melosh, H.J. and Sharp, T.G., 2020. Dwell time at high pressure of meteorites during impact ejection from Mars. *Icarus*, *343*, p.113689.

Brady J.B. and McCallister R.H. 1983. Diffusion data for clinopyroxenes from homogenization and self-diffusion experiments. *American Mineralogist*, *68*(1-2), pp.95-105.

Briani G., Gounelle M., Bourot-Denise M. and Zolensky M.E. 2012. Xenoliths and microxenoliths in H chondrites: Sampling the zodiacal cloud in the asteroid Main Belt. *Meteoritics & Planetary Science*, *47*(5), pp.880-902.

Chakraborty S. 2010. Diffusion coefficients in olivine, wadsleyite and ringwoodite. *Reviews in mineralogy and geochemistry*, *72*(1), pp.603-639.

Chen M., Sharp T.G., El Goresy A., Wopenka B. and Xie X. 1996. The majorite-pyrope+ magnesiowüstite assemblage: Constraints on the history of shock veins in chondrites. *Science*, *271*(5255), pp.1570-1573.

Chen M., El Goresy A. and Gillet P. 2004. Ringwoodite lamellae in olivine: Clues to olivine–ringwoodite phase transition mechanisms in shocked meteorites and subducting slabs. *Proceedings of the National Academy of Sciences*, *101*(42), pp.15033-15037.

Chen M., Li H., Goresy A.E., Liu J. and Xie X. 2006. Fracture-related intracrystalline transformation of olivine to ringwoodite in the shocked Sixiangkou meteorite. *Meteoritics & Planetary Science*, *41*(5), pp.731-737.

Chen M., Chen J., Xie X. and Xu J., 2007. A microstructural investigation of natural lamellar ringwoodite in olivine of the shocked Sixiangkou chondrite. *Earth and Planetary Science Letters*, *264*(1-2), pp.277-283.

Chen M. and Xie X. 2008. Two distinct assemblages of high-pressure liquidus phases in shock veins of the Sixiangkou meteorite. *Meteoritics & Planetary Science*, *43*(5), pp.823-828.

Cherniak D.J. and Dimanov A. 2010. Diffusion in pyroxene, mica and amphibole. *Reviews in Mineralogy and Geochemistry*, *72*(1), pp.641-690.

Christian J.W. 1975. The theory of transformations in metals and alloys. I. Equilibrium and general kinetic theory.

Coogan L.A., Hain A., Stahl S. and Chakraborty S. 2005. Experimental determination of the diffusion coefficient for calcium in olivine between 900 C and 1500 C. *Geochimica et Cosmochimica Acta*, *69*(14), pp.3683-3694.

Dimanov A. and Wiedenbeck M. 2006. (Fe, Mn)-Mg interdiffusion in natural diopside: effect of pO2. *European Journal of Mineralogy*, *18*(6), pp.705-718.

Dodd R.T. and Jarosewich E. 1979. Incipient melting in and shock classification of L-group chondrites. *Earth and Planetary Science Letters*, *44*(2), pp.335-340.

Dohmen R., Faak K. and Blundy J.D. 2017. Chronometry and speedometry of magmatic processes using chemical diffusion in olivine, plagioclase and pyroxenes. *Reviews in Mineralogy and Geochemistry*, *83*(1), pp.535-575.

Feng L., Miyahara M., Nagase T., Ohtani E., Hu S., El Goresy A. and Lin Y. 2017. Shock-induced PT conditions and formation mechanism of akimotoite-pyroxene glass assemblages in the Grove Mountains (GRV) 052082 (L6) meteorite. *American Mineralogist: Journal of Earth and Planetary Materials*, *102*(6), pp.1254-1262.

Ferroir T., Beck P., Van de Moortèle B., Bohn M., Reynard B., Simionovici A., El Goresy A. and Gillet P. 2008. Akimotoite in the Tenham meteorite: Crystal chemistry and high-pressure transformation mechanisms. *Earth and Planetary Science Letters*, *275*(1-2), pp.26-31.

Gaffey, M.J. and Fieber-Beyer, S.K., 2019, March. Is the (20) Massalia Family the source of the L-Chondrites. In *50th Lunar and Planetary Science Conference*.

Gail H.P. and Trieloff M. 2019. Thermal history modelling of the L chondrite parent body. *Astronomy & Astrophysics*, *628*, p.A77.

Gattacceca J., Krzesińska A.M., Marrocchi Y., Meier M.M., Bourot-Denise M. and Lenssen R. 2017. Young asteroid mixing revealed in ordinary chondrites: The case of NWA 5764, a polymict LL breccia with L clasts. *Meteoritics & Planetary Science*, *52*(11), pp.2289-2304.

Gillet, P. and Goresy, A.E., 2013. Shock events in the solar system: the message from minerals in terrestrial planets and asteroids. *Annual Review of Earth and Planetary Sciences*, *41*, pp.257-285.

Greshake, A., Fritz, J., Böttger, U. and Goran, D., 2013. Shear-induced ringwoodite formation in the Martian shergottite Dar al Gani 670. *Earth and Planetary Science Letters*, *375*, pp.383-394.

Hogrefe, A., Rubie, D.C., Sharp, T.G. and Seifert, F., 1994. Metastability of enstatite in deep subducting lithosphere. *Nature*, *372*(6504), pp.351-353.

Jenniskens P., Utas J., Yin Q.Z., Matson R.D., Fries M., Howell J.A., Free D., Albers J., Devillepoix H., Bland P. and Miller A. 2019. The Creston, California, meteorite fall and the origin of L chondrites. *Meteoritics & Planetary Science*, *54*(4), pp.699-720.

Jurewicz A.J. and Watson E.B. 1988. Cations in olivine, Part 2: Diffusion in olivine xenocrysts, with applications to petrology and mineral physics. *Contributions to Mineralogy and Petrology*, *99*(2), pp.186-201.

Kallemeyn G.W., Rubin A.E., Wang D. and Wasson J.T. 1989. Ordinary chondrites: Bulk compositions, classification, lithophile-element fractionations and composition-petrographic type relationships. *Geochimica et Cosmochimica Acta*, *53*(10), pp.2747-2767.

Kerschhofer L., Dupas C., Liu M., Sharp T.G., Durham W.B. and Rubie D.C. 1998. Polymorphic transformations between olivine, wadsleyite and ringwoodite: mechanisms of intracrystalline nucleation and the role of elastic strain. *Mineralogical Magazine*, *62*(5), pp.617-638.

Kerschhofer L., Rubie D.C., Sharp T.G., McConnell J.D.C. and Dupas-Bruzek C. 2000. Kinetics of intracrystalline olivine–ringwoodite transformation. *Physics of the Earth and Planetary Interiors*, *121*(1-2), pp.59-76.

Korochantseva E.V., Trieloff M., Lorenz C.A., Buykin A.I., Ivanova M.A., Schwarz W.H., Hopp J. and Jessberger E.K. 2007. L-chondrite asteroid breakup tied to Ordovician meteorite shower by multiple isochron 40Ar-39 Ar dating. *Meteoritics & Planetary Science*, *42*(1), pp.113-130.

Langenhorst F. and Poirier J.P. 2000. Anatomy of black veins in Zagami: clues to the formation of high-pressure phases. *Earth and Planetary Science Letters*, *184*(1), pp.37-55.

Litasov K.D. and Badyukov D.D. 2019. Raman Spectroscopy of High-Pressure Phases in Shocked L6 Chondrite NWA 5011. *Geochemistry International*, *57*(8), pp.912-922.

Liu M.C., McKeegan K.D., Harrison T.M., Jarzebinski G. and Vltava L., 2018. The Hyperion-II radio-frequency oxygen ion source on the UCLA ims1290 ion microprobe: Beam

characterization and applications in geochemistry and cosmochemistry. *International Journal of Mass Spectrometry, 424*, pp.1-9.

Malherbe J., Penen F., Isaure M.P., Frank J., Hause G., Dobritzsch D., Gontier E., Horréard F., Hillion F. and Schaumlöffel D. 2016. A new radio frequency plasma oxygen primary ion source on nano secondary ion mass spectrometry for improved lateral resolution and detection of electropositive elements at single cell level. *Analytical chemistry*, *88*(14), pp.7130-7136.

Marrocchi Y., Delbo M. and Gounelle M. 2021. The astrophysical context of collision processes in meteorites.

Meier, M.M., Welten, K.C., Riebe, M.E., Caffee, M.W., Gritsevich, M., Maden, C. and Busemann, H., 2017. Park Forest (L5) and the asteroidal source of shocked L chondrites. *Meteoritics & Planetary Science*, *52*(8), pp.1561-1576.

Melosh H.J. 1989. Impact cratering: A geologic process. *New York: Oxford University Press; Oxford: Clarendon Press*.

Miyahara M., El Goresy A., Ohtani E., Kimura M., Ozawa S., Nagase T. and Nishijima M. 2009. Fractional crystallization of olivine melt inclusion in shock-induced chondritic melt vein. *Physics of the Earth and Planetary Interiors*, *177*(3-4), pp.116-121.

Miyahara M., Ohtani E., Kimura M., El Goresy A., Ozawa S., Nagase T., Nishijima M. and Hiraga K. 2010. Coherent and subsequent incoherent ringwoodite growth in olivine of shocked L6 chondrites. *Earth and Planetary Science Letters*, *295*(1-2), pp.321-327.

Morbidelli A., Bottke W.F., Nesvorný D. and Levison H.F. 2009. Asteroids were born big. *Icarus*, *204*(2), pp.558-573.

Mosenfelder J.L., Marton F.C., Ross II C.R., Kerschhofer L. and Rubie D.C. 2001. Experimental constraints on the depth of olivine metastability in subducting lithosphere. *Physics of the Earth and Planetary Interiors*, *127*(1-4), pp.165-180.

Nesvorný, D., Vokrouhlický, D., Morbidelli, A. and Bottke, W.F., 2009. Asteroidal source of L chondrite meteorites. *Icarus*, *200*(2), pp.698-701.

Ohtani E., Kimura Y., Kimura M., Takata T., Kondo T. and Kubo T. 2004. Formation of high-pressure minerals in shocked L6 chondrite Yamato 791384: constraints on shock conditions and parent body size. *Earth and Planetary Science Letters*, *227*(3-4), pp.505-515.

Price G.D., Putnis A. and Agrell S.O. 1979. Electron petrography of shock-produced veins in the Tenham chondrite. *Contributions to Mineralogy and Petrology*, *71*(2), pp.211-218.

Sawamoto H. 1987. Phase diagram of MgSiO3 at pressures up to 24 GPa and temperatures up to 2200 C: phase stability and properties of tetragonal garnet. *High-pressure research in mineral physics*, *209*, p.219.

Schmitz B., Tassinari M. and Peucker-Ehrenbrink B. 2001. A rain of ordinary chondritic meteorites in the early Ordovician. *Earth and Planetary Science Letters*, *194*(1-2), pp.1-15.

Sharp T.G., Lingemann C.M., Dupas C. and Stöffler D. 1997. Natural occurrence of MgSiO3-ilmenite and evidence for MgSiO3-perovskite in a shocked L chondrite. *Science*, *277*(5324), pp.352-355.

Spandler C. and O'Neill H.S.C. 2010. Diffusion and partition coefficients of minor and trace elements in San Carlos olivine at 1,300 C with some geochemical implications. *Contributions to Mineralogy and Petrology*, *159*(6), pp.791-818.

Stöffler D., Keil K. and RD S.E. 1991. Shock metamorphism of ordinary chondrites. *Geochimica et Cosmochimica Acta*, *55*(12), pp.3845-3867.

Stöffler, D., Hamann, C. and Metzler, K., 2018. Shock metamorphism of planetary silicate rocks and sediments: Proposal for an updated classification system. *Meteoritics & Planetary Science*, *53*(1), pp.5-49.

Strom, C.A., Fieber-Beyer, S.K., Gaffey, M.J. and Germann, J.T., 2021, March. A Spectral Analysis of the Massalia Asteroid Family to Evaluate the L-Chondrite Source Hypothesis. In *Lunar and Planetary Science Conference* (No. 2548, p. 1597).

Swindle T.D., Kring D.A. and Weirich J.R. 2014. 40Ar/39Ar ages of impacts involving ordinary chondrite meteorites. *Geological Society, London, Special Publications*, *378*(1), pp.333-347.

Tomioka N. and Fujino K. 1997. Natural (Mg, Fe) SiO3-ilmenite and-perovskite in the Tenham meteorite. *Science*, *277*(5329), pp.1084-1086.

Tomioka, N. and Fujino, K., 1999. Akimotoite,(Mg, Fe) SiO3, a new silicate mineral of the ilmenite group in the Tenham chondrite. *American Mineralogist*, *84*(3), pp.267-271.

Tomioka N. 2007. A model for the shear mechanism in the enstatite-akimotoite phase transition. *Journal of Mineralogical and Petrological Sciences*, *102*(4), pp.226-232.

Tomioka N. and Miyahara M. 2017. High-pressure minerals in shocked meteorites. *Meteoritics & Planetary Science*, *52*(9), pp.2017-2039.

Tschauner O., Ma C., Beckett J.R., Prescher C., Prakapenka V.B. and Rossman G.R. 2014. Discovery of bridgmanite, the most abundant mineral in Earth, in a shocked meteorite. *Science*, *346*(6213), pp.1100-1102.

Wang H., Li Y., Zhang F. and Lin C. 1995. SEM Studies on the Chemical and Petrologic Features of Taizhou (L-5) Chondrite in China. In *Lunar and Planetary Science Conference* (Vol. 26).

Wang W. and Takahashi E. 1999. Subsolidus and melting experiments of a K-rich basaltic composition to 27 GPa: Implication for the behavior of potassium in the mantle. *American Mineralogist*, *84*(3), pp.357-361.

Wlotzka F. 1990. The Meteoritical Bulletin. *Meteoritics*, *25*(3), pp.237-239.

Xie Z., Sharp T.G. and DeCarli P.S. 2006. High-pressure phases in a shock-induced melt vein of the Tenham L6 chondrite: Constraints on shock pressure and duration. *Geochimica et Cosmochimica Acta*, *70*(2), pp.504-515.

Zhang A., Hsu W., Wang R. and Ding M. 2006. Pyroxene polymorphs in melt veins of the heavily shocked Sixiangkou L6 chondrite. *European Journal of Mineralogy*, *18*(6), pp.719-726.

8. Tables

Table 1: EPMA representative analysis of minerals, glass and matrix in Acfer040, Tenham and Sixiangkou (meaned value over 3 crystals). Values are in wt.%. Detection limit is ~0.02 wt.%.

Acfer 040	Al2O3	CaO	Cr2O3	FeO	MgO	MnO	NaO	SiO2	TiO2	Total
Ringwoodite	0.07	0.07	0.10	24.99	38.22	0.19	0.10	37.29	0.05	101.08
Akimotoite	0.21	0.49	0.14	8.78	34.13	0.26	0.15	55.84	0.26	100.27
$MgSiO_3$ Glass	0.23	1.15	0.13	18.83	23.76	0.76	2.01	51.90	0.18	98.95
Matrix	0.87	1.32	0.56	9.96	28.44	0.66	2.14	52.19	0.22	96.37
Maskelynite	21.28	2.55	0.09	1.52	1.46	0.05	8.05	63.70	0.07	98.76
Tenham	**Al2O3**	**CaO**	**Cr2O3**	**FeO**	**MgO**	**MnO**	**NaO**	**SiO2**	**TiO2**	**Total**
Ringwoodite	0.05	0.04	6.47	23.27	37.20	0.40	0.06	38.07	0.04	105.59
Akimotoite	0.19	0.83	0.17	14.40	28.66	0.45	0.39	54.02	0.18	99.30
Low Ca Pyroxene	0.20	0.61	0.15	13.52	28.60	0.47	0.23	54.41	0.22	98.41
High Ca Pyroxene	0.44	21.67	1.15	5.29	16.03	0.21	0.50	52.88	0.49	98.67
Matrix	4.54	2.43	0.54	12.85	23.96	0.40	1.27	49.79	0.17	95.95
Maskelynite	22.78	2.65	0.07	0.88	0.42	0.07	5.36	64.86	0.08	97.17
Sixiangkou	**Al2O3**	**CaO**	**Cr2O3**	**FeO**	**MgO**	**MnO**	**Na2O**	**SiO2**	**TiO2**	**Total**
Ringwoodite	n.d.	0.03	0.02	23.59	38.13	0.38	0.05	37.98	0.02	100.19
Olivine	n.d.	0.04	0.01	22.84	38.41	0.49	0.00	38.39	n.d.	100.14
Akimotoite	0.14	0.76	0.07	15.44	28.22	0.49	0.42	53.37	0.20	99.11
Low Ca Pyroxene	0.14	0.76	0.11	14.25	29.05	0.49	0.17	54.99	0.20	100.15
Maskelynite	22.77	2.00	0.01	0.21	0.01	0.00	3.79	68.73	0.03	98.35

Table 2: Diffusion distances measured from NanoSIMS diffusion profiles and lamellae width measured by SEM.

Meteorite	Diffusion Distance (µm)	Std.	n	Lamellae/Crystal Width (µm)	Error	n
Tenham (Ringwoodite)	2.4	0.13	118	2.2	0.48	26
Sixiangkou (Ringwoodite)	1.4	0.4	21	1.2	0.1	5
Acfer 040 (Akimotoite)	3.34	0.56	75	3.32	0.24	67

n = Number of analyses std= standard deviation

Table 3: Akimotoite-melt empirical partition coefficients calculated from compositional data from Acfer 040.

Element	Partition Coefficient
Fe	0.46
Mg	1.28
Mn	0.33
Ca	0.45
Na	0.30
Si	1.10

Table 4: Crystal growth, diffusion coefficients and other constants used in the modelling.

Coefficient	Value	Source
Ea (Mn) – oliv.	218 kJ	Jurewicz et al 1988, Beck et al 2005
D0 (Mn) - oliv	$10^{-7.167}$ m^2s^{-1}	Jurewicz et al 1988, Beck et al 2005
Ea (Ca) - oliv	176 kJ	Jurewicz et al 1988, Beck et al 2005
D0 (Ca) -oliv	$10^{-9.155}$ m^2s^{-1}	Jurewicz et al 1988, Beck et al 2005
Ea (Fe) -Px	297 kJ	Dimanov and Wiedenbeck 2006
D0 (Fe) - Px	$1.62*10^{-6}$ m^2s^{-1}	Dimanov and Wiedenbeck 2006
Ea (Ca) - Px	361 kJ	Brady and McCallister 1983
D0 (Ca) - Px	$3.9*10^{-7}$ m^2s^{-1}	Brady and McCallister 1983
ΔGa	266 kJ/mol	Kerschhofer et al., 2000
k0	$5.63*10^{-4}$ $m.s^{-1}.K^{-1}$	Kerschhofer et al., 2000
$\Delta H°$	30200 J/mol	Akaogi et al., 1989
$-\Delta S°$	-14.75kJ/molK	Akaogi et al., 1989
V	4.165 cm^3/mol	Navrotsky et al 1995, Xie et al 2006
v	5km/s	Bottke et al 1994

9. Figures

Figure 1:
BSE images of various textures found in our shocked melt veins. Rw stands for ringwoodite, Aki for akimotoite, Px for pyroxene, Ol for olivine, Maj for Majorite, Ahr for ringwoodite so enriched in iron it is closer to the Ahrensite endmember. A) Intergrown olivine and ringwoodite with an iron rich crown, possibly Ahrensite (left), and aggregates of ringwoodite (right), in Acfer 040. B) Discontinuous ringwoodite lamellae in an olivine crystal in the veins of Sixiangkou. C) An aggregate of akimotoite in a pyroxene crystal, in the Sixiangkou meteorite. D) A pyroxene crystal surrounded by olivine and presenting lighter akimotoite lamellae, Tenham meteorite. E) A partially molten pyroxene crystal presenting akimotoite in the veins of Acfer 040. F) Assemblage of majorite and glassy pyroxene (right), with akimotoite (left) in the veins of Acfer 040.

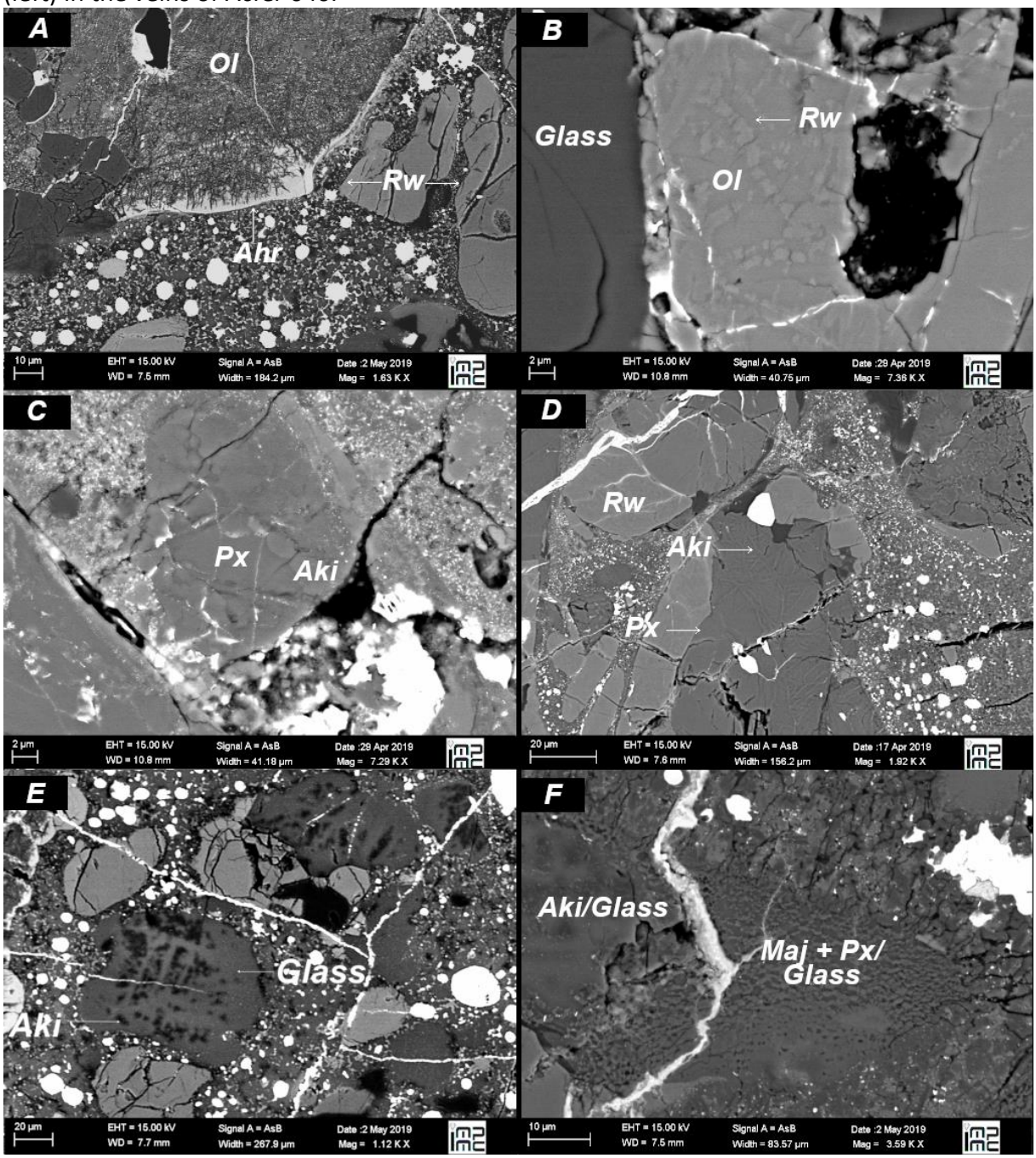

Figure 2:

A) STEM image of ringwoodite lamellae in Tenham. Appearing in lighter colors are the lamellae, including a set of thinner, coherent ones, as well as a larger, heterogenous one, composed of a finely crystalline center surrounded by larger crystals. B) STEM image of the "Glassy formation" - Akimotoite crystals (lighter) embedded in a $MgSiO_3$ glass.

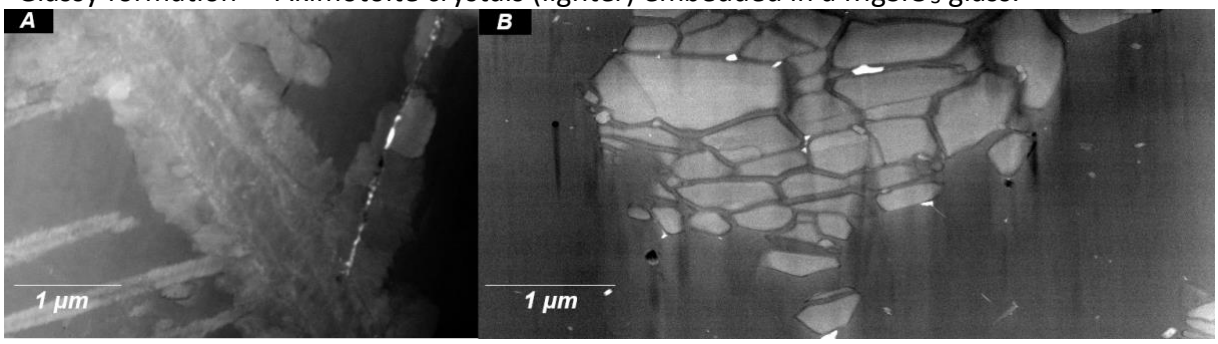

Figure 3: Characteristic Long Exposure Raman spectra of various high-pressure minerals observed in the veins of the Tenham meteorite.

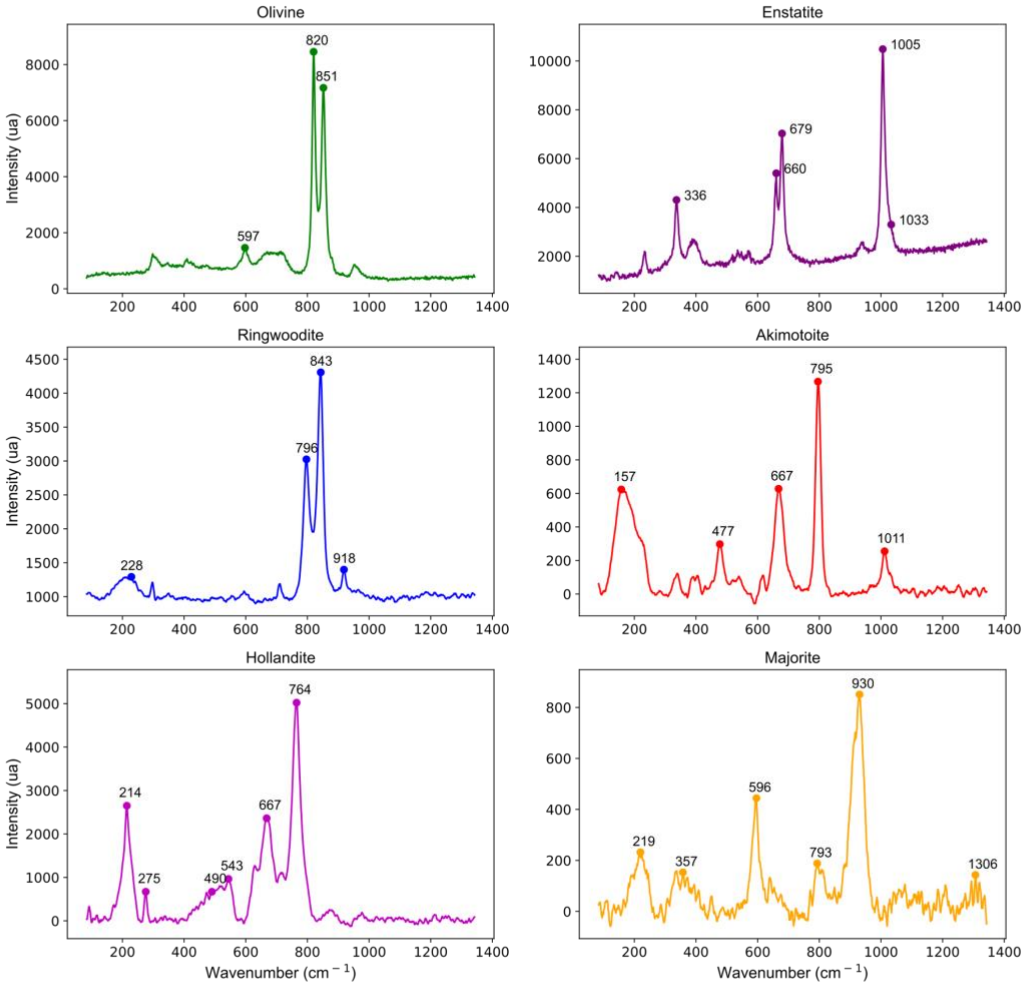

Figure 4: Comparisons of elemental profiles by TEM (magenta) and NanoSIMS (Mn: green, Mg: blue, Fe: black, Ca: red, Na: pink). The envelopes represent the instrument error. These profiles were taken on exactly the same assemblages on the same FIB sections. Local discrepancies could be due to sample contamination during the transportation from the TEM to the NanoSIMS, as well as ablation or amorphization of the samples (see main text).

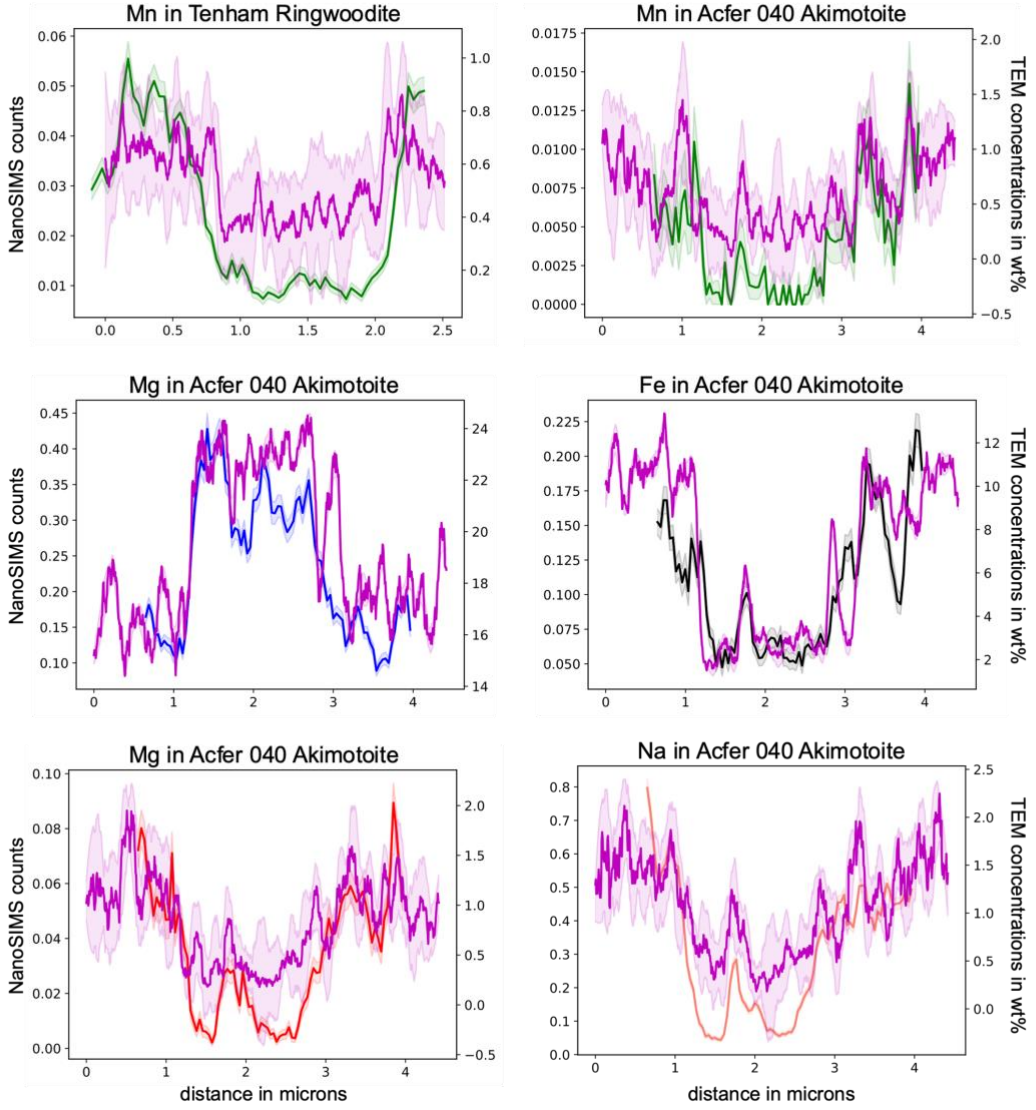

Figure 5: STEM-EDX Profiles of Mn, Mg, Si and Fe in the larger ringwoodite lamellae of Tenham. All profiles were taken along the red line. The lighter part is the lamellae of ringwoodite, and the darker crystal in the host olivine.

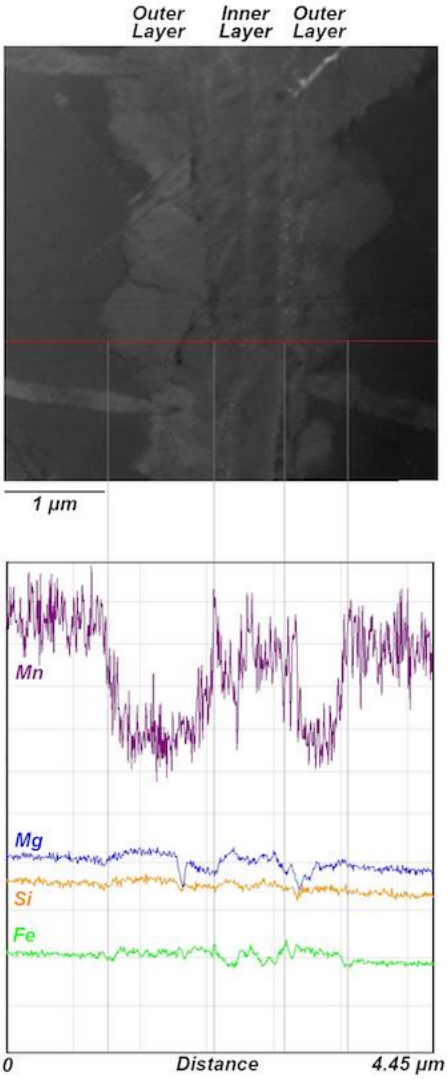

Figure 6: A) Example of a NanoSIMS image corresponding to figure 1.B. The lamellae (center) are depleted in ^{55}Mn. B) EMPA image of the iron concentration in an akimotoite-glass assemblage in the veins of Acfer 040 (arrow).

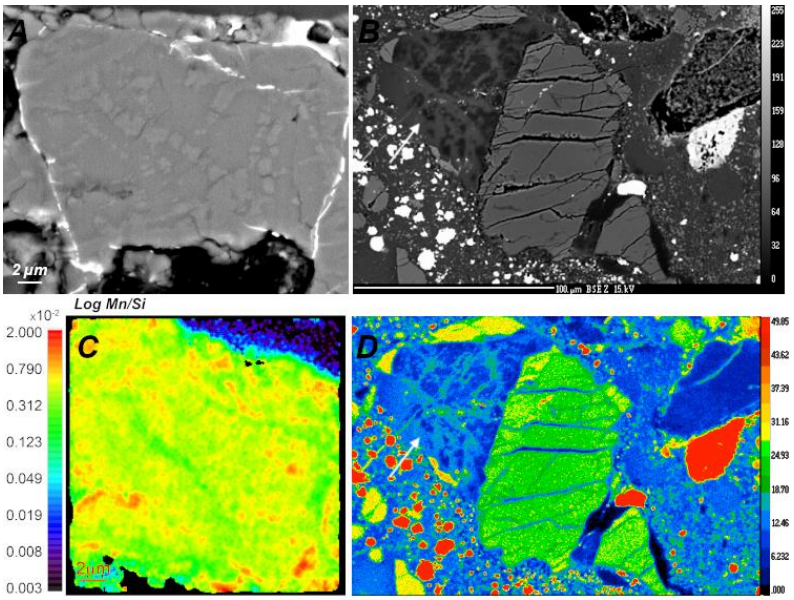

Figure 7: Results of the shock pulse model as a function of the characteristic shock temperature. The colored curves correspond to the diffusion of different elements. The black curves correspond to the timescale determinations via growth rate (see discussion for calculation details).